

# Thesis Title

by

E. Ross



A thesis submitted to the  
University of Birmingham  
for the degree of  
DOCTOR OF PHILOSOPHY

Solar and Stellar Physics Group (SASP)

School of Physics and Astronomy

University of Birmingham

Birmingham, B15 2TT

Month 20XX

# Contents

<b>List of Figures</b>	<b>iii</b>
<b>List of Tables</b>	<b>iv</b>
<b>List of Abbreviations</b>	<b>vi</b>
<b>1 Introduction</b>	<b>1</b>
1.1 Space Weather . . . . .	1
1.1.1 Background . . . . .	1
1.1.2 Impacts of Space Weather . . . . .	3
1.2 Cosmic Rays . . . . .	7
1.2.1 Background . . . . .	7
1.2.2 Cosmic Rays in the Atmosphere . . . . .	10
1.2.3 Cosmic Ray Detectors . . . . .	12
1.2.4 Cosmic Ray Observations of Space Weather . . . . .	15
1.3 The HiSPARC Experiment . . . . .	21
1.3.1 HiSPARC Project . . . . .	21
1.3.2 HiSPARC Detector and Station Configuration . . . . .	22
1.4 The Solar Magnetic Field/Activity/Features... . . . .	27
1.4.1 ... . . . .	27
1.5 Thesis Structure . . . . .	28
<b>Bibliography</b>	<b>29</b>

# List of Figures

1.1	UK National Risk Register for hazards, diseases, accidents, and societal risks showing space weather as a medium-high risk ( <a href="#">Cabinet Office, 2017</a> ) . . . . .	4
1.2	The sources and effects of space weather. Impacts are shown including loss of telecommunications and GNSS, increased radiation levels, and ground induced currents (ESA/Science Office, <a href="#">CC BY-SA 3.0 IGO</a> ) .	5
1.3	Cosmic ray differential energy spectrum using data measured by several experiments. The inset shows the H/He ratio at constant rigidity ( <a href="#">Zyla, P. A. (Particle Data Group) et al., 2020</a> ) . . . . .	9
1.4	The original Simpson’s 12-pile NM is shown on the left and the modern NM64 is shown on the right in its 6-tube configuration ( <a href="#">Kang et al., 2012</a> ) . . . . .	13
1.5	Schematic design of a typical scintillation muon detector with back-end electronics ( <a href="#">Gloeckler, 2010</a> ) . . . . .	14
1.6	A two-step Forbush decrease measured at three NM stations, Deep River, Mt. Wellington, Kerguelen, in July 1982 ( <a href="#">Cane, 2000</a> ). The thicker black line indicates the average of the count rates from the three stations. Arrows show the start of the two decreases caused by the shock and the ICME ejecta. . . . .	16
1.7	A schematic diagram of an ICME-driven FD taken from <a href="#">Cane (2000)</a> . It shows the different cosmic ray responses from two paths, indicated by A and B. A experiences the shock and ejecta, therefore experiencing a two-step FD; B only experiences the shock, therefore experiencing a single decrease. The time of shock passage is indicated by a solid, vertical line marked, S; the start and end times of ejecta passage are indicated by vertical, dashed lines marked T1 and T2, respectively. . . . .	17
1.8	A GLE measured at nine NM stations in October 1989 ( <a href="#">Cramp, J. L. et al., 1997</a> ). . . . .	18
1.9	A schematic diagram of the ‘garden hose’ field line taken from <a href="#">Duldig et al. (1993)</a> . . . . .	20
1.10	Schematic diagram of the HiSPARC scintillation detector. (A): PMT; (B): light-guide adaptor; (C): light-guide; (D): scintillator. . . . .	23
1.11	Typical formations of two-detector and four-detector stations. In each, the grey circle denotes a GPS antenna which is located in between the detectors to provide a precise timestamp for each signal. . .	24

- 1.12 (a): An example PMT signal after digital conversion by the HiSPARC electronics box. The horizontal lines denote: the noise cut-off (dotted line), which is used for setting a limit when integrating the pulse height, to give the pulse integral; the low-voltage threshold (dash-dot); the high-voltage threshold (dashed). (b) The pulse height distribution over the course of a single day from HiSPARC station 501. The vertical lines show the low-voltage threshold (dash-dot) and the high-voltage threshold (dashed). . . . . 26

# List of Tables

- 1.1 Most prominent decay modes of the mesonic components of CR air showers and of muons. Note:  $K^-$  modes are charge conjugates of the decay modes below ([Zyla, P. A. \(Particle Data Group\) et al., 2020](#)) . 11

# List of Abbreviations

**AR** Active Region.

**AS** Air Shower.

**BiSON** Birmingham Solar Oscillations Network.

**CIR** Corotating Interaction Region.

**CMB** Cosmic Microwave Background.

**CME** Coronal Mass Ejection.

**CR** Cosmic Ray.

**EAS** Extensive Air Shower.

**FD** Forbush Decrease.

**FE** Forbush Effect.

**FEID** Forbush Effects and Interplanetary-disturbances Database.

**GCR** Galactic Cosmic Ray.

**GIC** Ground Induced Current.

**GLE** Ground Level Enhancement.

**GNMN** Global Neutron Monitor Network.

**GNSS** Global Navigation Satellite System.

**GZK** Greisen-Zatsepin-Kuzmin.

**HiSPARC** High School Project on Astrophysics and Research with Cosmics.

**ICME** Interplanetary Coronal Mass Ejection.

**IMF** Interplanetary Magnetic Field.

**MD** Muon Detector.

**MIP** Minimum Ionising Particle.

**MOSWOC** Met Office Space Weather Operations Centre.

**MPV** Most Probable Value.

**NM** Neutron Monitor.

**NOAA** National Oceanic and Atmospheric Administration.

**PCR** Primary Cosmic Ray.

**PMMA** Polymethylmethacrylate.

**PMT** Photo Multiplier Tube.

**SCR** Solar Cosmic Ray.

**SEP** Solar Energetic Particle.

**SMMF** Solar Mean Magnetic Field.

**SRB** Solar Radio Burst.

**SSN** Sun Spot Number.

**SWPC** Space Weather Prediction Center.

**UHECR** Ultra-High-Energy Cosmic Ray.

# 1 Introduction

*While the majority of this chapter was written for the thesis, parts of Sec ?? were written for ? and have been adapted from the introduction in that work to limit repetition. **YOU WANT SOMETHING LIKE THIS AT THE START OF EACH SCIENCE CHAPTER TOO, TO SHOW WHAT YOU DID AND ANY ACKNOWLEDGEMENTS OF OTHER PEOPLE***

## 1.1 Space Weather

### 1.1.1 Background

Space weather is defined as ([Cannon & Royal Academy of Engineering \(Great Britain\), 2013](#)):

*variations in the Sun, solar wind, magnetosphere, ionosphere, and thermosphere, which can influence the performance and reliability of a variety of space-borne and ground-based technological systems and can also endanger human health and safety.*

Space weather phenomena have been observed for hundreds of years, mainly through observations of the aurorae, but its impacts are slowly becoming more tangible in modern civilisation, as we grow reliant on electronics ([Beggan et al., 2018](#)).

There are two main sources of space weather: (i) those that are solar in nature and (ii) those whose origins are external to the solar system but penetrate into the heliosphere. Space weather manifests itself broadly in three ways:



1. Electromagnetic radiation: which space weather is generally linked with an enhancement in the output of the Sun’s spectrum.
2. Magnetic fields / plasma: which can cause disturbances in the solar wind and the magnetosphere.
3. Energetic charged particles: which refer to ionising charged particles and ions.

The arrival of these space weather outputs at Earth depends on the type and energy. Likewise, the solar storms induced differ, however the general chronology of events was outlined by [Cannon & Royal Academy of Engineering \(Great Britain\) \(2013\)](#):

1. Storms begin with the evolution of one or more complex sunspot groups and Active Regions (ARs) on the solar surface.
2. Within ARs, one or more solar flares occur and the electromagnetic radiation are detected on Earth within approximately 8 minutes.
3. Solar Energetic Particles (SEPs) are released and are measured at Earth, both using satellites and ground-based detectors, within approximately 15 minutes. SEPs continue to arrive over a period of several hours – days.
4. A Coronal Mass Ejection (CME) occurs and propagates outwards, arriving at a distance of 1 AU within  $\sim 15 - 72$  hours. The impact on Earth depends on the CME speed, how close it passes to Earth, and the orientation of the magnetic fields, with Southward magnetic field generating the most severe geomagnetic storms because of its interference with Earth’s Northward magnetic field resulting in reconnection at the magnetopause.

The largest documented space weather event since modern records began occurred in 1859, the solar super storm known as the “Carrington event”. The available measurements of this event are limited to geomagnetic field perturbations, as

well as eye witness accounts of solar brightening and aurorae ([Cannon & Royal Academy of Engineering \(Great Britain\), 2013](#)). However, recently cosmonuclide measurements from ice cores have been used to learn about the Carrington event and it is believed that the large solar flare around this period exceeded class X10 ([Riley, 2012](#)).

Since the beginning of the space age there have been no other super storms, however there have been large storms that have affected the infrastructure and caused a large economic impact. The consensus is that another storm of the Carrington event level is inevitable and could significantly impact society. There is a view that a Carrington-like event may occur again in a period of 250 years with a confidence of  $\sim 95\%$  and within a period of 50 years with a confidence of  $\sim 50\%$  ([Cannon & Royal Academy of Engineering \(Great Britain\), 2013](#)); however it is stressed that these figures should be interpreted with care. It was suggested by [Riley \(2012\)](#) that a Carrington-like event may occur with  $\sim 12\%$  probability within between 2012-2022 and later in 2012 a large storm occurred, missing Earth, but it strongly interacted with the STEREO-A satellite. This near miss highlights that Carrington-level events are a real threat to society and that we need a method of predicting their occurrence, arrival, and impact.

### **1.1.2 Impacts of Space Weather**

Space weather is an increasingly tangible threat to modern infrastructure and society, due to the increasing reliance on electronic technology. In 2011 space weather was added to the UK National Risk Assessment for the first time, and the subsequent National Risk Register in 2012 ([BIS, 2015](#)) where it has remained to-date ([Government, 2020](#)). At the time of writing this thesis space weather risk was rated as a medium severity/high likelihood risk; at the same level as emerging infectious diseases, poor air quality, and heatwaves (see Figure 1.1) ([Cabinet Office, 2017](#)).

An alarming aspect of Figure 1.1 is that the likelihood of space weather events

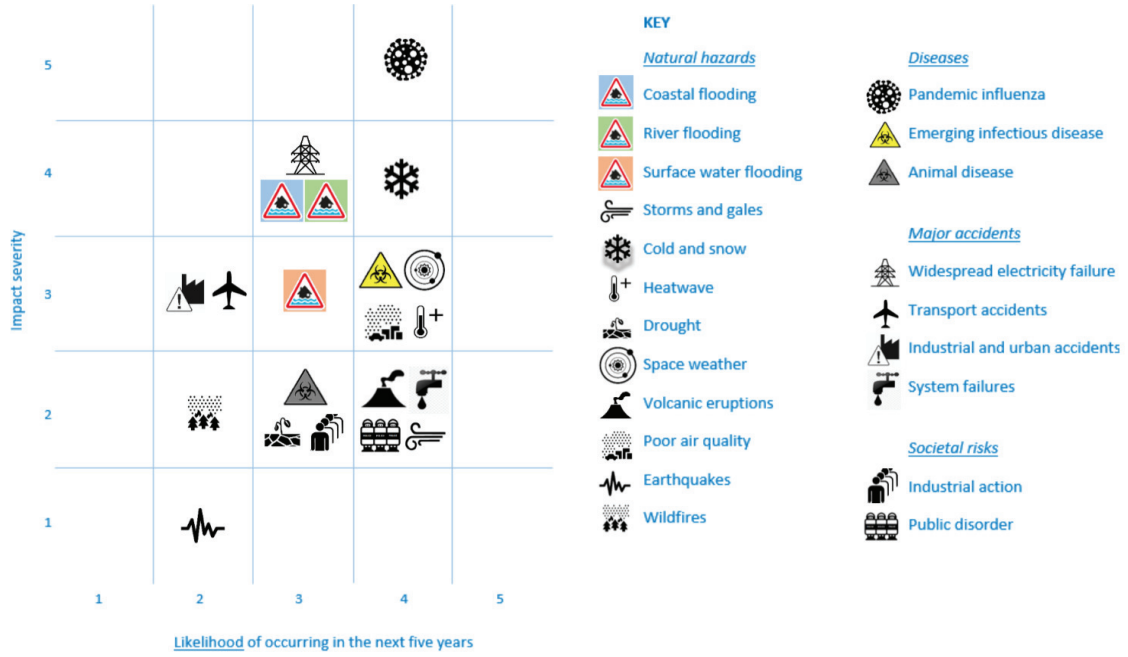


Figure 1.1: UK National Risk Register for hazards, diseases, accidents, and societal risks showing space weather as a medium-high risk ([Cabinet Office, 2017](#))

occurring in 5 years from 2017 was rated the same as pandemic influenza. Finishing this Ph.D. during a global pandemic highlights the importance of taking this risk register very seriously. We should learn from the global response to the COVID-19 pandemic and ensure that the world has a resolute plan to deal with the occurrence of a severe space weather event.

There are many ways that technological systems are impacted by space weather both on or above ground and Figure 1.2 displays many of the key impacts that we know of ([Beggan et al., 2018](#)).

As far back as October 1841 it was reported that a solar storm was responsible for railway disruptions around Exeter, due to magnetic disturbances making it impossible to ascertain whether the onward line was clear, leading to sixteen minute delays ([Nature, 1871](#)).

It is possible for space weather events to induce geomagnetic storms that can cause damaging Ground Induced Currents (GICs) within large power grids causing them to fail. Two such famous cases of GIC grid failures are the cases in Quebec,

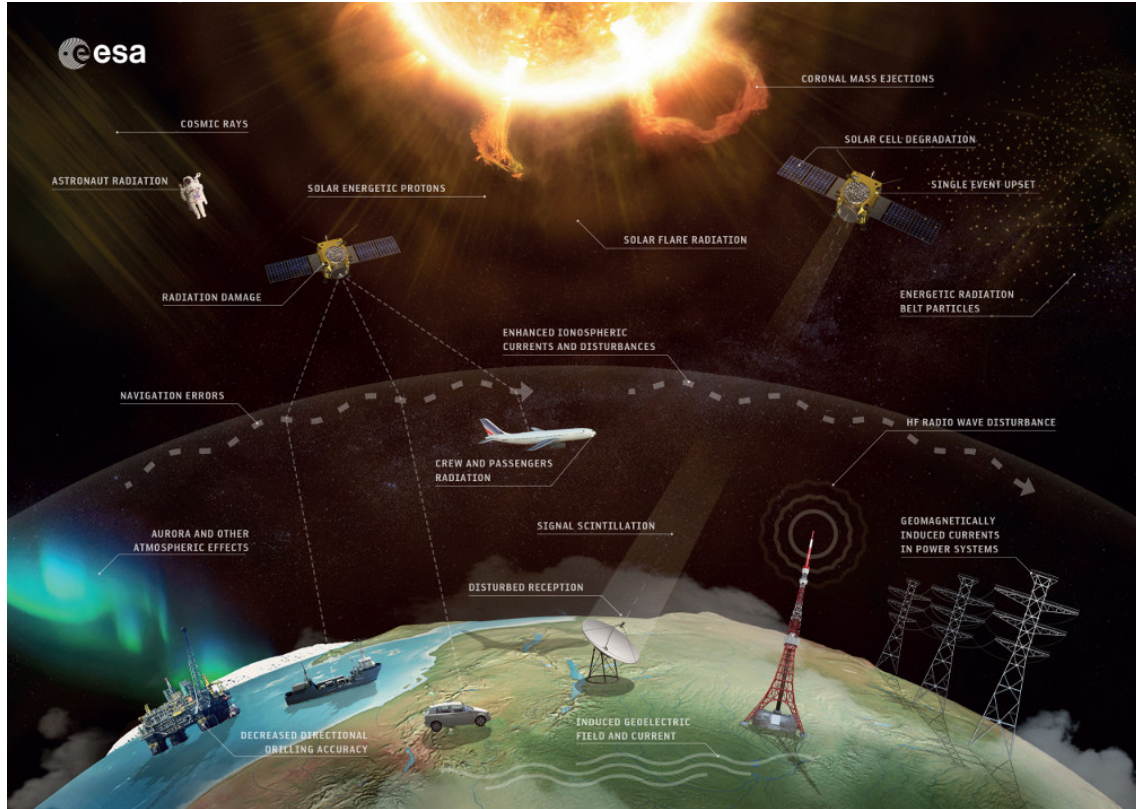


Figure 1.2: The sources and effects of space weather. Impacts are shown including loss of telecommunications and GNSS, increased radiation levels, and ground induced currents (ESA/Science Office, [CC BY-SA 3.0 IGO](#))

Canada in 1989 which resulted in the failure of the Quebec-Hydro grid for 9 hours, and the city-wide black-out in Malmö, Sweden during the Halloween storm in 2003 ([Viljanen, 2011](#); [Beggan et al., 2018](#)).

It is documented that in May 1967 the U.S. Air Force were close to engaging in conflict with its enemies during those politically tense times as Solar Radio Bursts (SRBs) induced radio frequency interference was nearly misinterpreted as surveillance jamming, an act of war, if it hadn't have been that the U.S. had begun investing in space environment monitoring and were able determine that space weather was really the cause ([Knipp et al., 2016](#)). Furthermore, in more modern times, scintillation effects induced in the ionosphere affect Global Navigation Satellite System (GNSS) communications which has a large societal effect due to our reliance on GNSS ([Cannon & Royal Academy of Engineering \(Great Britain\), 2013](#)) as shown

in Figure 1.2.

Solar storms are also responsible for creating sudden increases in ionising radiation which at typical flight altitudes can lead to the risk of malfunctions in aircraft microelectronic systems and unquantified radiation doses to passengers and crew ([Cannon & Royal Academy of Engineering \(Great Britain\), 2013](#)). In orbit these conditions threaten the operation of satellites and the safety of manned space endeavours which is of particular concern with the current ambitions to return to the Moon and venture to Mars.

There are even concerns that major storms could cause radiation increases at the Earth's surface, Ground Level Enhancements (GLEs), which may cause malfunctions in microelectronics that are likely to be of increasing concern in the design of safety-critical systems ([Cannon & Royal Academy of Engineering \(Great Britain\), 2013](#)).

Finally, a cost analysis estimated a present-day total U.S. economic cost for a super storm on the scale of the 1859 Carrington event ([Homeier & Wei, 2013](#)). The cost estimated is heavily dependent on the duration of outages, the damages caused, and the availability of spare parts for repair; however they estimated the impact on the U.S. economy to be at around \$0.6-2.6 trillion ([Homeier & Wei, 2013](#)). These figures show the large scale impact that space weather can have on the economy and that mitigation techniques to reduce this cost are of imperative necessity.

Due to the many ways that space weather can impact civilisation, and that it is predicted that there is a significant probability of the re-occurrence of large solar storms, it is easy to understand why space weather forecasting is becoming increasingly more necessary as a mitigation technique.

The U.S. National Oceanic and Atmospheric Administration (NOAA) is the leading global space weather forecasting agency. The NOAA Space Weather Prediction Center (SWPC) gathers data in real-time to describe the conditions of the sun, heliosphere, magnetosphere, and ionosphere to understand the environment within

the heliosphere and on Earth. With this data, the SWPC produces forecasts, warnings, and alerts available to inform anyone concerned and affected by space weather ([NOAA, 2018](#)).

Since the addition of space weather to the UK risk register, the UK Met Office Space Weather Operations Centre (MOSWOC) opened in 2014 ([BIS, 2015](#)). MOSWOC is mandated to produce daily space weather forecasts and is therefore developing a forecasting infrastructure using ground-based and satellite instrumentation to monitor space weather events. In addition scientific research at MOSWOC is carried out to better understand the physical processes involved in space weather phenomena to improve forecasting accuracy and lead-times; current forecasting enables prediction of CMEs impacting Earth to within only plus or minus six hours at best ([MetOffice, 2013](#)).

Forecasting and predicting is one aspect of the response to severe space weather events. We must also learn from the global response to the COVID-19 pandemic and ensure that upon the occurrence of a severe space weather event, suitable pre-planning has been performed and a sufficient contingent action is planned.

[discussion of the time of arrival of certain space weather...??]

## 1.2 Cosmic Rays

### 1.2.1 Background

Cosmic Rays (CRs) are charged particles and atomic nuclei with energies spanning from keV up to around  $10^{21}$  eV, that encroach upon the Earth from all directions ([Giacalone, 2010](#)). It is understood that CRs are composed of  $\sim 99\%$  of atomic nuclei and  $\sim 1\%$  electrons ([Gaisser et al., 2016](#)); of the atomic nuclei  $\sim 87\%$  are protons,  $\sim 12\%$  are  $\alpha$ -particles, and a smaller contribution are heavier nuclei of around  $\sim 1\%$  ([Gruppen, 2005](#); [Dunai, 2010](#); [Zyla, P. A. \(Particle Data Group\) et al., 2020](#)). CRs mainly originate from outside the solar system, known as Galactic Cosmic Rays (GCRs) ([Zyla, P. A. \(Particle Data Group\) et al., 2020](#)). These GCRs mostly

originate from within the Milky Way, although they are also expected to originate from extra-galactic sources, in particular for CRs with energies above  $10^{18}$  eV (Aab et al., 2017). Incoming low-energy CRs ( $\lesssim 1$  GeV/nucleon) are modulated by the solar wind, which decelerates GCRs and can even forbid lower-energy GCRs from the inner solar system (Grupen, 2005). Consequently, there exists a strong anti-correlation between solar activity and the GCRs flux (Zyla, P. A. (Particle Data Group) et al., 2020).

Cosmic rays produced within the heliosphere are mostly of a solar origin, known as Solar Cosmic Rays (SCRs) or SEPs. These SCRs are generally of a lower energy than GCRs and may be accelerated in the solar wind, by interplanetary shocks, or in solar eruptions (e.g. solar flares) (Giacalone, 2010). SCRs have typical energies in the order of magnitude range of  $\sim 10^1$  keV –  $\sim 1$  GeV (Chilingarian, 2003; Bruno et al., 2018).

The intensity spectrum of Primary Cosmic Rays (PCRs) in the energy range from  $10^9$  eV to  $\sim 10^{14}$  eV is given approximately by:

$$I_N(E) = \frac{dN}{dE} \approx 1.8 \times 10^4 (E/1 \text{ GeV})^{-\alpha} \frac{\text{nucleons}}{\text{m}^2 \text{ s sr GeV}}, \quad (1.1)$$

where  $E$  is the energy per nucleon (including rest mass energy) in GeV and  $\alpha = 2.7$  is the differential spectral index of the cosmic-ray flux (Zyla, P. A. (Particle Data Group) et al., 2020).

Above the spectrum ‘knee’ ( $\sim 10^{15} - 10^{16}$  eV) the spectral index is thought to increase to  $\sim 3$  (Zyla, P. A. (Particle Data Group) et al., 2020). At even higher energies, in the region of the spectrum ‘ankle’ ( $\sim 10^{18.5}$  eV) the spectral index reduces and the spectrum becomes less steep. This is in the regime of Ultra-High-Energy Cosmic Rays (UHECRs) and the interaction between GCRs and photons of the Cosmic Microwave Background (CMB) sets an upper limit on their energy, the Greisen-Zatsepin-Kuzmin (GZK) limit (Zyla, P. A. (Particle Data Group) et al., 2020). The GZK limit implies that CRs with energies exceeding  $\sim 5 \times 10^{19}$  eV



must have originated from distances within a horizon of  $\sim 50$  Mpc, as otherwise their energy would have been reduced by the GZK effect (Zyla, P. A. (Particle Data Group) et al., 2020).

Figure 1.3 shows a graphical representation of the CR energy spectrum described by equation (1.1) for a number of CR species over the energy range  $10^{-1} - 10^6$  GeV/nucleus by the measured flux of CRs measured by several different experiments.

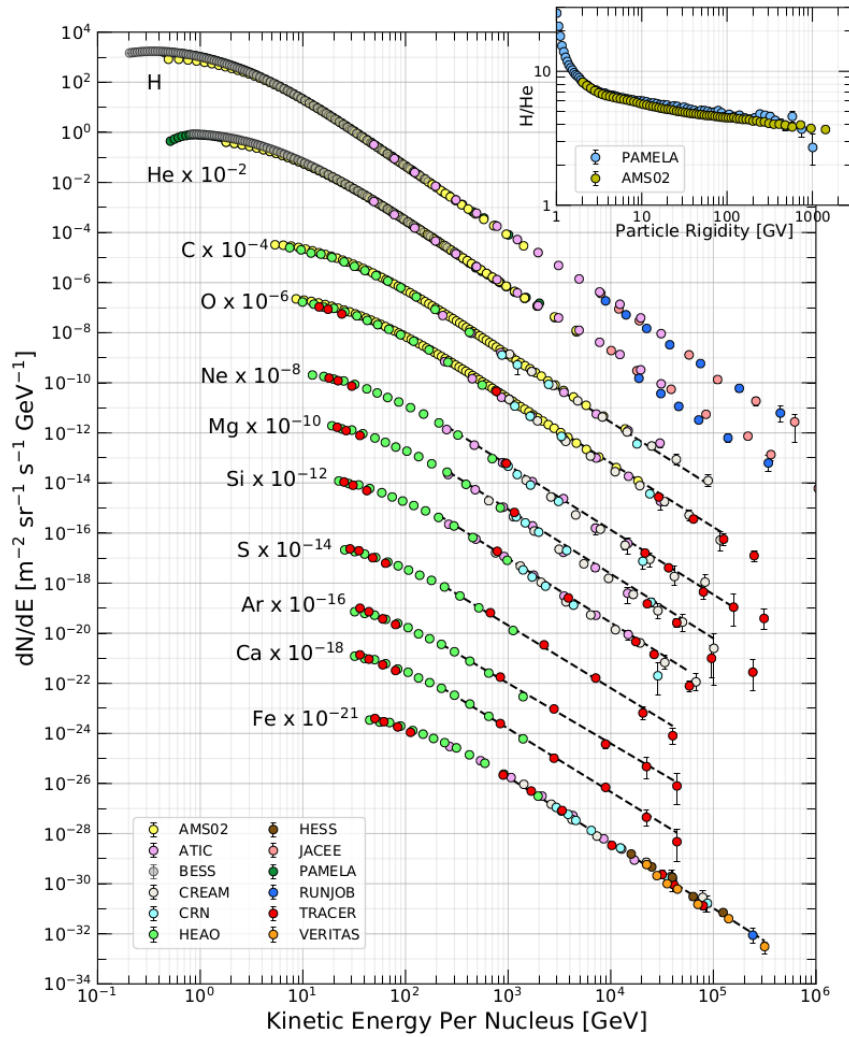


Figure 1.3: Cosmic ray differential energy spectrum using data measured by several experiments. The inset shows the H/He ratio at constant rigidity (Zyla, P. A. (Particle Data Group) et al., 2020)

Propagation of CRs through magnetic fields depends on their gyroradius or Lar-



mor radius (Zyla, P. A. (Particle Data Group) et al., 2020). Therefore a common description of CRs uses a property called the *magnetic rigidity* which is defined by:

$$R = r_L B c = \frac{p c}{Z e} \quad (1.2)$$

where  $r_L$  is the Larmor radius,  $B$  is the magnetic field strength,  $c$  is the speed of light,  $p$  is the particle’s momentum,  $Z$  is the atomic number, and  $e$  is the electron charge. The magnetic rigidity has units Volts (V), or usually due to the large magnitude, Gigavolts (GV). The rigidity is used to describe CRs as particles with different charges and masses have the same dynamics in a magnetic field if they have the same rigidity (Zyla, P. A. (Particle Data Group) et al., 2020).

### 1.2.2 Cosmic Rays in the Atmosphere

CRs in the interstellar medium traverse a very low-density medium, but experience a much denser environment when they reach the atmosphere. The typical mean free path of protons in the atmosphere is  $\sim 90 \text{ g cm}^{-2}$ , which mean the first interactions of CRs occur in the upper layers of the atmosphere, at a height of  $\sim 15 - 20 \text{ km}$  (Grupen, 2005).

The PCR will predominantly interact with the atmospheric nuclei via strong interactions (Grupen, 2005). When PCR interact with atmospheric nuclei, the interaction leads to the production of a cascade of secondary particles. The secondary particles can also undergo interaction or decay, producing tertiary particles, and the process continues until all the particles’ energy become insufficient to create new particles. If a concentrated, large number of secondary particles reach ground-level, the cascade of particles is called an Air Shower (AS), or an Extensive Air Shower (EAS) for extremely high numbers of secondary particles, which can have a footprint area of several  $\text{km}^2$ . The AS is often described as being a cone, with the base being the shower front and the apex being the primary CR.

Hadronic cascade components (or the “hard component” of ASs) are produced by

CR protons and nuclei interacting with atmospheric nuclei. This process typically produces lower energy protons, neutrons, pions, and kaons. In this thesis we are mostly interested in the muonic air shower development (see Section 1.3), so here we will focus on the development of the mesons in the ASs, as they predominantly produce muons. In Table 1.1, the most likely modes of decay for air shower mesons are shown with the branching ratio for each mode. In addition, we also show the most likely decay modes of muons Table 1.1.

Table 1.1: Most prominent decay modes of the mesonic components of CR air showers and of muons. Note:  $K^-$  modes are charge conjugates of the decay modes below (Zyla, P. A. (Particle Data Group) et al., 2020)

Decay mode	Branching ratio
$\pi^+ \rightarrow \mu^+ + \nu_\mu$	$99.98770 \pm 0.00004\%$
$\pi^- \rightarrow \mu^- + \bar{\nu}_\mu$	$99.98770 \pm 0.00004\%$
$\pi^0 \rightarrow \gamma + \gamma$	$98.823 \pm 0.034\%$
$\pi^0 \rightarrow e^+ + e^- + \gamma$	$1.174 \pm 0.035\%$
$K^+ \rightarrow \mu^+ + \nu_\mu$	$63.56 \pm 0.11\%$
$K^+ \rightarrow \pi^+ + \pi^0$	$20.67 \pm 0.08\%$
$K^+ \rightarrow \pi^+ + \pi^+ + \pi^-$	$5.583 \pm 0.024\%$
$K^+ \rightarrow \pi^0 + e^+ + \nu_e$	$5.07 \pm 0.04\%$
$K^+ \rightarrow \pi^0 + \mu^+ + \nu_\mu$	$3.352 \pm 0.033\%$
$K^+ \rightarrow \pi^+ + \pi^0 + \pi^0$	$1.760 \pm 0.023\%$
$\mu^+ \rightarrow e^+ + \nu_e + \bar{\nu}_\mu$	$\sim 100\%$
$\mu^- \rightarrow e^- + \bar{\nu}_e + \nu_\mu$	$\sim 100\%$

Due to the short lifetimes of pions and kaons,  $\sim 26$  ns and  $\sim 12$  ns, respectively (Zyla, P. A. (Particle Data Group) et al., 2020), they decay during their journey to ground-level. It is shown in Table 1.1 that the most probable decay modes involve the production of muons. Muons are the most abundant charged particles at ground level. Most muons are produced high in the atmosphere ( $\sim 15$  km) and lose about 2 GeV to ionization before reaching the ground and the mean energy of muons at the ground is  $\sim 4$  GeV (Zyla, P. A. (Particle Data Group) et al., 2020).

In addition to the hadronic component of an air shower, electron and photon

constituents of cascades are called the electromagnetic component (or “soft component”). These are typically initiated by electrons and photons under the processes of Bremsstrahlung (Gruppen, 2005),

$$e \rightarrow e + \gamma, \quad (1.3)$$

or pair production (Gruppen, 2005),

$$\gamma^* \rightarrow e^- + e^+. \quad (1.4)$$

Ionisation losses mean that electrons and positrons lose energy rapidly until they either annihilate or recombine with nuclei, and photons lose their energy by being either absorbed in scattering and/or the photoelectric effect. Therefore most of the electrons, positrons, and photons observed at ground level are produced from the decaying hadronic AS component and muon decay is the dominant source of low-energy electrons at ground level (Zyla, P. A. (Particle Data Group) et al., 2020).

Finally, there is a minimum rigidity cut-off which implies that the energy of any PCR must exceed a minimum energy to be able to initiate an AS or particle cascade and be measured at ground-level. This limit is dependent on the depth of the atmosphere above the detector, but is greatest at sea-level and decreases with increasing altitude. The minimum energy to be measured at sea-level is  $\sim 430$  MeV/nucleon (Dorman, 2004a,b; Poluianov et al., 2017).

### 1.2.3 Cosmic Ray Detectors

To observe CRs there are many types of usable detectors, both ground-based and space-based (Schrijver & Siscoe, 2010); in this thesis we are mostly concerned with ground-based detectors of the AS hadronic component. The most common type of ground-based CR detectors are Neutron Monitors (NMs) and Muon Detectors (MDs) which indirectly measure CR particles through the secondary particles produced in

CR cascades.

## Neutron Monitors

The neutron monitor, invented by [Simpson \(1948\)](#), has been extensively used for CR observations of the space environment ([Clem & Dorman, 2000](#)). The NM is an example of an ionisation detector whereby energetic neutrons encounter a nucleus within a gas, producing charged, secondary particles which in turn ionise the surrounding gas.

The original “IGY” NM design made use of a paraffin reflector to trap slow neutrons within the detector, a producer material (typically lead) which multiplied the number of slow neutrons registered by the detector in order to amplify the signal, a moderator to further slow neutrons, and cylindrical proportional counters utilising  $\text{BF}_3$  gas ([Simpson, 1948](#); [Simpson et al., 1953](#)). A schematic diagram of the detector is shown in Figure 1.4a.

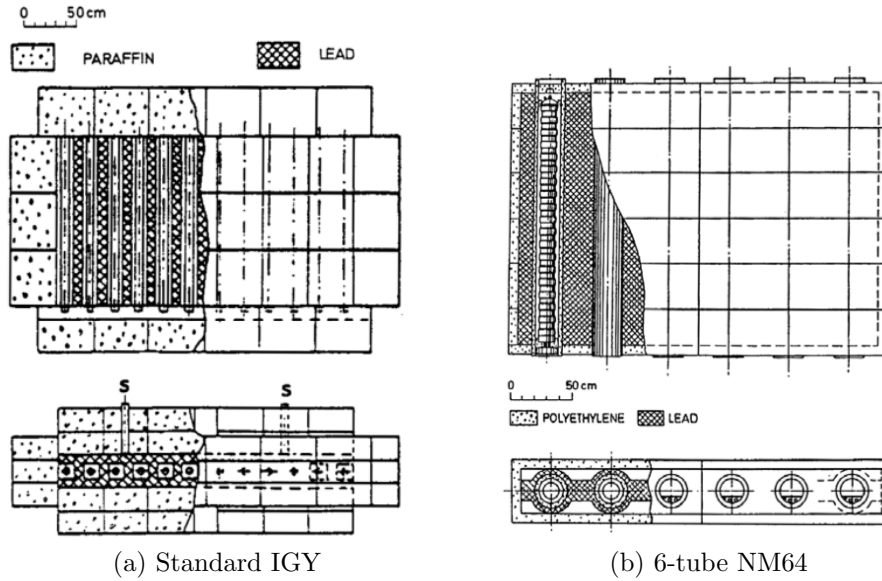


Figure 1.4: The original Simpson’s 12-pile NM is shown on the left and the modern NM64 is shown on the right in its 6-tube configuration ([Kang et al., 2012](#))

An improved “NM64” NM design is now the preferred detector type, which makes use of a polyethylene reflector, lead producer, polyethylene moderator, and  $^{10}\text{BF}_3$  or  $^3\text{He}$  gas-filled cylindrical proportional counters. A schematic diagram of

the detector is shown in Figure 1.4b. The new design provided an improvement over the IGY design by a factor of about 3.3 in the count rate per unit area of producer (Stoker et al., 2000); however the choice of  $^{10}\text{BF}_3$  gas or  $^3\text{He}$  gas does not significantly affect the detector performance (Kang et al., 2012).

## Muon Detectors

Muon detectors are an example of a scintillation detector, whereby light emitted by atoms excited in a medium is collected and converted into an electrical signal. The scintillation medium can be solid, liquid, or gas; however solid scintillation detectors are attractive as they have a higher electron density (Gloeckler, 2010).

A general design of a MD is shown in Figure 1.5. When an energetic particle passes through a scintillator material, some of the particle's energy is lost in ionising the scintillator material and the scintillator material releases photons. The light pipe directs the photons towards a Photo Multiplier Tube (PMT) where a cascade of electrons are produced and the resulting electrical signal is amplified and recorded through the back-end electronics.

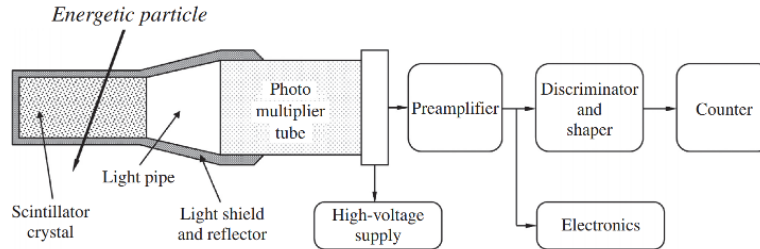


Figure 1.5: Schematic design of a typical scintillation muon detector with back-end electronics (Gloeckler, 2010)

Desirable properties of scintillator materials are a high conversion efficiency, transparency to the light that they emit, short fluorescent decay times, and spectral distributions suitable for photosensitive devices (Gloeckler, 2010).

A range of different material types are used in scintillator detectors however the most common scintillator materials for MDs are organic scintillators consisting of aromatic hydrocarbons (the fluors) in a solid plastic solvent (the base). Energetic

particles traversing the scintillator excite the base rather than the fluor due to the low fluor density. The plastic base however has a low yield and is not transparent to its own scintillation light; thus the fluor is added to therefore increase the yield of this popular type of scintillator (Fokkema, 2012).

### 1.2.4 Cosmic Ray Observations of Space Weather

There have been many documented observations of space weather events using CR detectors. The most notable types of CR space weather effects are Forbush Decreases (FDs) and GLEs. Here we discuss the properties of each.

#### Forbush Decreases

Short-term decreases in the GCR flux were first observed by Forbush (1937) and therefore were later coined as FDs or Forbush Effects (FEs). FDs are characterised by a sharp decrease in GCR intensity over a period of several hours – days, followed by a gradual recovery taking place over several days – a week (Cane, 2000; Belov, 2008; Wawrzynczak & Alania, 2010), as shown in Figure 1.6.

There are two FD origins: one caused by Corotating Interaction Regions (CIRs) (Dumbović et al., 2016), and one caused by Interplanetary Coronal Mass Ejections (ICMEs) and the shocks they drive (Belov, 2008). The biggest FDs (magnitudes  $> 5\%$ ) are strictly associated with ICMEs (Belov et al., 2001). Of the kind caused by ICMEs, the majority of are produced by ICMEs with speeds in the range  $400 - 1200 \text{ km s}^{-1}$  (Lingri et al., 2016); the typical speed of the solar wind is, for slow solar wind, in the range:  $300 - 400 \text{ km s}^{-1}$ , and for fast solar wind,  $\sim 750 \text{ km s}^{-1}$  (Owens & Forsyth, 2013). Previous literature has also shown that the type cause by CIRs produce recurrent, more symmetric, and lower-amplitude decreases (Dumbović et al., 2012), while the type caused by ICMEs result in the more strongly asymmetric decreases as shown in Figure 1.6 (Lockwood, 1971; Cane, 2000; Dumbović et al., 2012). In addition the ICME-driven FDs typically result in a two-step FD, where the first step of the decrease is due to the passage of the leading shock and the

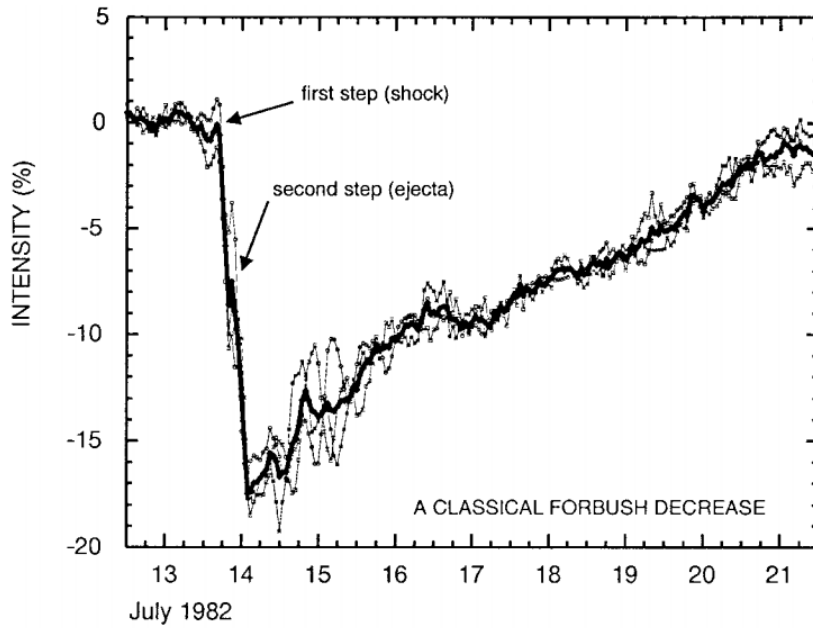


Figure 1.6: A two-step Forbush decrease measured at three NM stations, Deep River, Mt. Wellington, Kerguelen, in July 1982 (Cane, 2000). The thicker black line indicates the average of the count rates from the three stations. Arrows show the start of the two decreases caused by the shock and the ICME ejecta.

second step is due to the ICME itself, as shown in Figure 1.7 (Cane, 2000).

FDs exhibit a rigidity dependence on their amplitudes which is approximately related to  $R^{-\gamma}$  where the exponent ranges from  $0.4 \lesssim \gamma \lesssim 1.2$  (Lockwood, 1971). In addition, Belov et al. (2001, 2014) showed the magnitude of the FD is proportional to the speed, mass, and width of the CME.

The Forbush Effects and Interplanetary-disturbances Database (FEID)<sup>1</sup> is a record of all the FDs observed since the beginning of the Global Neutron Monitor Network (GNMN) (Belov, 2008). The total number of events is  $\sim 7630$  during the epoch 1957 –2020. Many studies have discussed the observations of FDs using this data and investigate their features, driving factors, and precursors; for an overview see: Belov et al. (2001); Usoskin et al. (2008); Wawrzynczak & Alania (2010); Rockenbach et al. (2014); Arunbabu et al. (2015).

<sup>1</sup><http://spaceweather.izmiran.ru/eng/dbs.html>

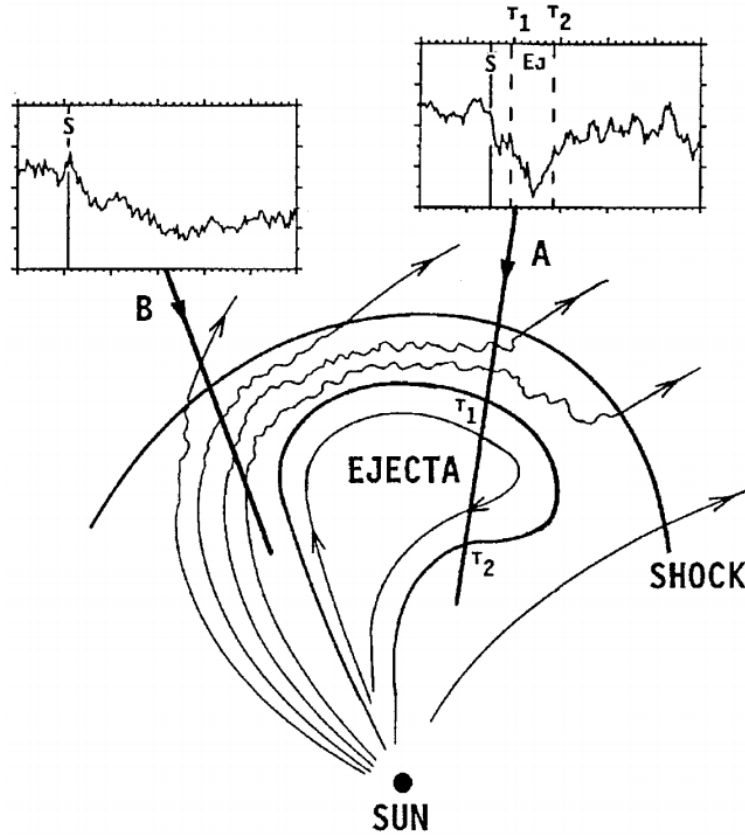


Figure 1.7: A schematic diagram of an ICME-driven FD taken from [Cane \(2000\)](#). It shows the different cosmic ray responses from two paths, indicated by A and B. A experiences the shock and ejecta, therefore experiencing a two-step FD; B only experiences the shock, therefore experiencing a single decrease. The time of shock passage is indicated by a solid, vertical line marked, S; the start and end times of ejecta passage are indicated by vertical, dashed lines marked T1 and T2, respectively.

## Ground Level Enhancements

Short-term increases in the GCR flux were first observed in the 1940s and early 1950s, but it wasn't until after the largest recorded event, in September 1956, that these increases were defined as GLEs ([Cramp, 1996](#)). GLEs are the detection of an increased number of the highest-energy portion ( $> 500$  MeV, [Kuwabara et al. \(2006b\)](#)) of SEPs arriving at Earth along lines of Interplanetary Magnetic Field (IMF) following a solar eruptive event ([McCracken et al., 2012](#); [Poluianov & Usoskin, 2017](#)). The SEPs, which cause GLEs, can cause serious damage to satellite electronics and are a hazard to air crew and astronauts; hence, the monitoring of these events are of importance for space weather forecasting. GLEs are characterised by



a sharp rise in CR intensity over a period of several minutes – hours, followed by a gradual decay taking place over several hours, as shown in Figure 1.8.

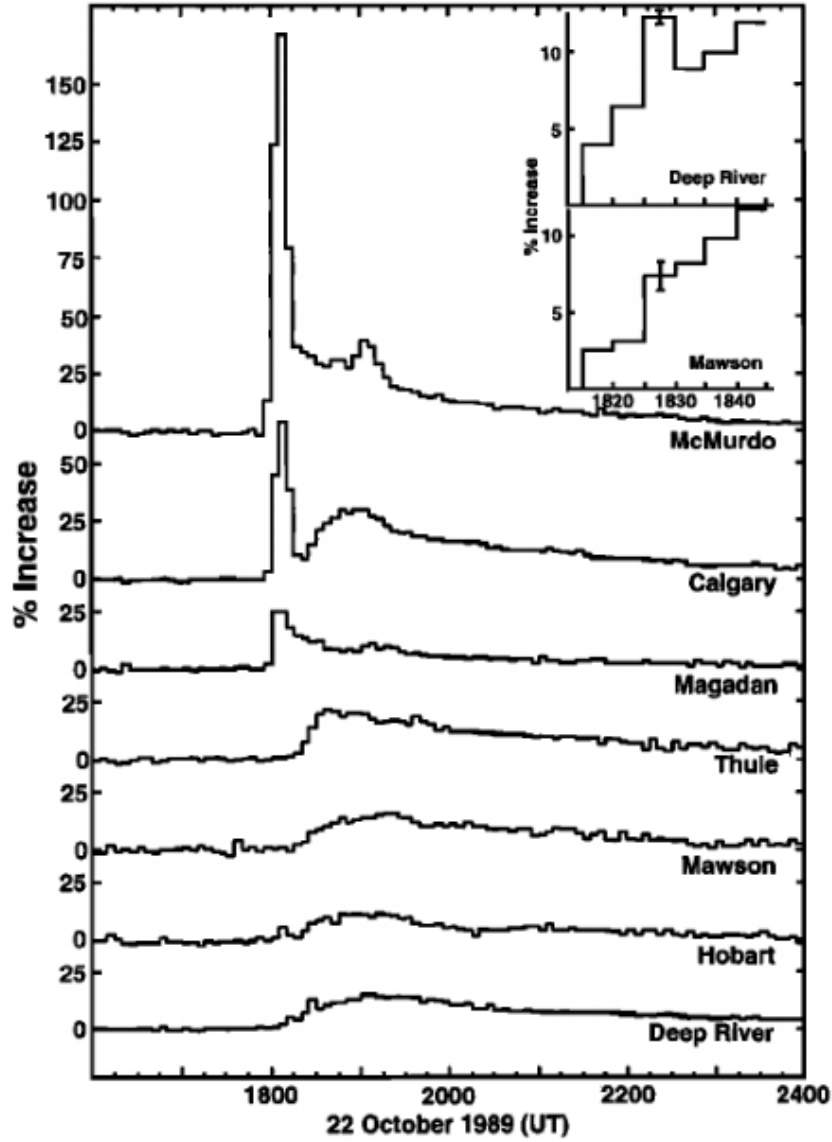


Figure 1.8: A GLE measured at nine NM stations in October 1989 (Cramp, J. L. et al., 1997). ...

The total number of GLEs observed to-date is low, there have been only 72. The GLE database<sup>2</sup> is a record of events starting from GLE 5 (February 1956), since the beginning of the GNMN (Usoskin et al., 2016). Many studies have discussed the observations of GLEs, investigating their features as well as the spectra and

<sup>2</sup><https://gle oulu.fi>

anisotropy of PCRs that produce the GLEs; for an overview see: [Shea & Smart \(1982\)](#); [Cramp \(1996\)](#); [Belov et al. \(2010\)](#); [McCracken et al. \(2012\)](#); [Strauss et al. \(2017\)](#); [Mishev et al. \(2018\)](#). [Strauss et al. \(2017\)](#) analysed the shapes of fourteen GLEs and showed the existence of a linear dependence between the rise and decay times:  $\tau_d \approx 3.5\tau_r$ .

[discuss the drivers behind GLEs, i.e. flares and coronal holes...]

The solar magnetic field is ‘frozen’ into the solar wind plasma. As the Sun rotates, so do the IMF lines which forms the Parker spiral [!! CITE !!]. A field line connecting the Sun to the Earth exists which stems from the western limb of the Sun, at a longitude of about  $60^\circ$ . This is known as the ‘garden hose’ field line. Charged particles follow magnetic field lines and therefore SEPs that are accelerated in flares located near to the solar end of the ‘garden hose’ field line usually arrive promptly and have very sharp onsets ([Duldig et al., 1993](#); [Andriopoulou et al., 2011](#)). This causes a strong anisotropy in the arrival directions of the early SEPs inducing GLEs, and the anisotropy is shown in Figure 1.8, whereby McMurdo, Calgary, and Magaden NM stations observed an earlier GLE onset, with a high magnitude, than the other stations ([Duldig et al., 1993](#); [Cramp, J. L. et al., 1997](#)). Conversely, GLEs associated with flares far from the ‘garden hose’ field line are usually delayed in their arrival at Earth, due to having to cross magnetic field lines, and have more gradual increases to maximum intensity ([Duldig et al., 1993](#)). Very few GLEs have originated far away from the base of the ‘garden hose’ at the solar surface ([Duldig et al., 1993](#); [Andriopoulou et al., 2011](#)).

The accepted definition of a GLE, since the 1970s has been ([Poluianov et al., 2017](#)):

*A GLE event is registered when there are near-time coincident and statistically significant enhancements of the count rates of at least two differently located NMs.*

However, recently a newer GLE definition has been adopted due to the increase

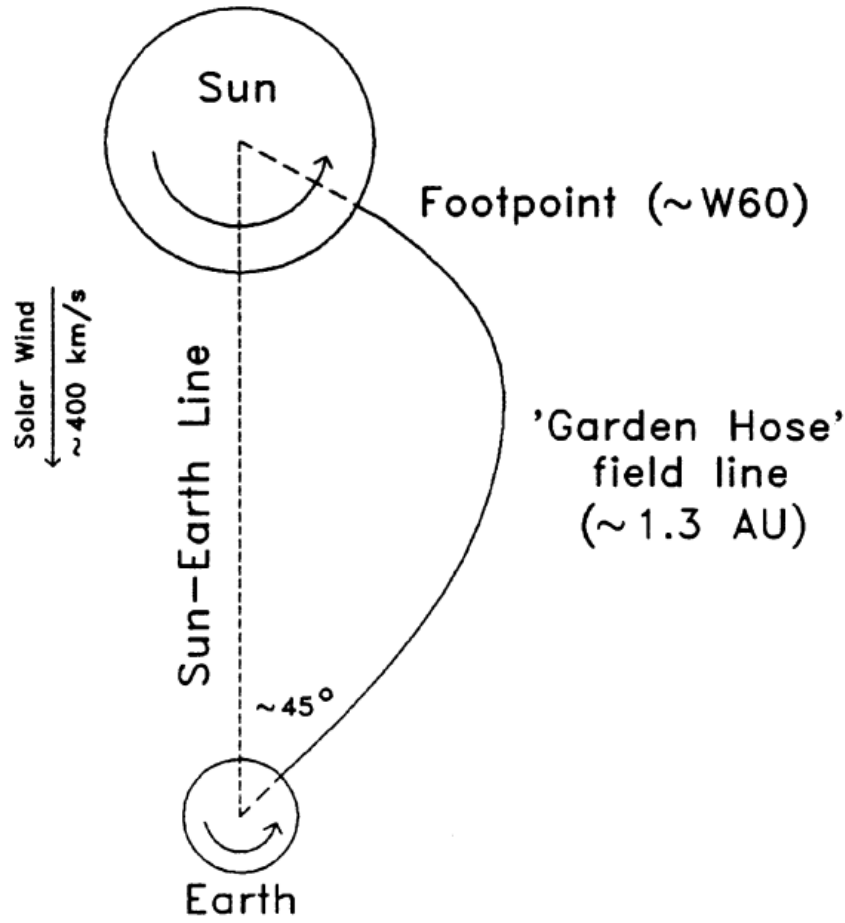


Figure 1.9: A schematic diagram of the ‘garden hose’ field line taken from [Duldig et al. \(1993\)](#).

in the number of NM stations that are more sensitive to lower energy CRs due to their high latitudes (i.e. in near-polar regions) or higher altitudes. It is a concern that these new NM stations will classify many more GLEs than their near-sea-level counterparts; thus affecting the homogeneity of the current list of GLEs ([Poluianov et al., 2017](#)). Therefore the new GLE definition is as follows ([Poluianov et al., 2017](#)):

*A GLE event is registered when there are near-time coincident and statistically significant enhancements of the count rates of at least two differently located neutron monitors, including at least one neutron monitor near sea-level and a corresponding enhancement in the proton flux measured by a space-borne instrument(s).*

The new definition therefore invoked the introduction of a sub-GLE, defined as

([Poluianov et al., 2017](#)):

*A sub-GLE event is registered when there are near-time coincident and statistically significant enhancements of the count rates of at least two differently located high-elevation neutron monitors and a corresponding enhancement in the proton flux measured by a space-borne instrument(s), but no statistically significant enhancement in the count rates of neutron monitors near sea level.*

Finally, a GLE real-time alarm system was developed by [Kuwabara et al. \(2006a,b\)](#), using data from NMs and MDs, which has been shown to provide the earliest alert for the onset of SEP-driven space weather events. They showed their alerts provide a warning up to an hour earlier than the storm onset. Furthermore, they also show that through utilising the GNMN, monitoring precursory anisotropy, they can also issue warnings several hours ahead of near-Earth, in-situ satellite observations. They state that using both NMs and MDs provides a dual energy range for observations, providing a more effective system.

## 1.3 The HiSPARC Experiment

### 1.3.1 HiSPARC Project

The High School Project on Astrophysics and Research with Cosmics (HiSPARC) stands for is a scientific outreach project that was initiated in the Netherlands in 2002 ([Bartels, 2012](#)). The HiSPARC project has two main goals: the study of UHECR for astroparticle physics research, and to serve as a resource to expose high school students to scientific research ([Bartels, 2012](#)).

HiSPARC is a global network of muon detectors spread across the Netherlands, Denmark, the UK, and Namibia. The detectors at each station record muon counts and may be used for many scientific experiments, such as: reconstruction of the direction of a cosmic ray induced air shower, reconstruction of the energy of the air

shower’s primary particle, investigation between the atmospheric conditions and the number of cosmic rays observed, etc.

Data recorded by the HiSPARC stations are stored and are available publicly at <http://www.hisparc.nl>, where the CR counts, atmospheric data, station meta-data, and more can be found.

### 1.3.2 HiSPARC Detector and Station Configuration

The detection philosophy of HiSPARC is to sample the footprints of EASs using coincident triggers between scintillation detectors. As HiSPARC was set up as an outreach programme for high schools, this impacted detector design. Resources are limited in schools and the detectors are usually financed by the participating high schools, colleges, and universities. In addition, students (accompanied by their teachers and local node support staff) are responsible for assembly and installation their detectors, which are typically installed on the roofs of schools. Due to this, the detectors needed to be cheap, robust, and easily maintainable, therefore the scintillation detector was selected for the HiSPARC network.

Scintillators consist of materials that emit light when charged particles pass through them with sufficient energy to ionise the scintillator material. The total light produced is proportional to the number of charged particles, and can be collected by a PMT. Each HiSPARC detector utilises a plastic scintillator of dimensions 1000 mm x 500 mm x 20 mm, providing a detection area of 0.5 m<sup>2</sup>. A vertically incident Minimum Ionising Particle (MIP) has a most probable energy loss in 2 cm of the scintillation material of 3.51 MeV ( $\equiv$  1 MIP) ([van Dam et al., 2020](#)).

The scintillator is glued to a triangular/‘fish-tailed’ light-guide (dimensions, base: 500 mm; top: 25 mm; height: 675 mm), and a light-guide adapter provides the optical interface between the square end of the light-guide and the cylindrical aperture of the PMT. The configuration of a single HiSPARC detector is shown in Figure 1.10.

The scintillator is made of a material consisting of polyvinyltoluene as the base,

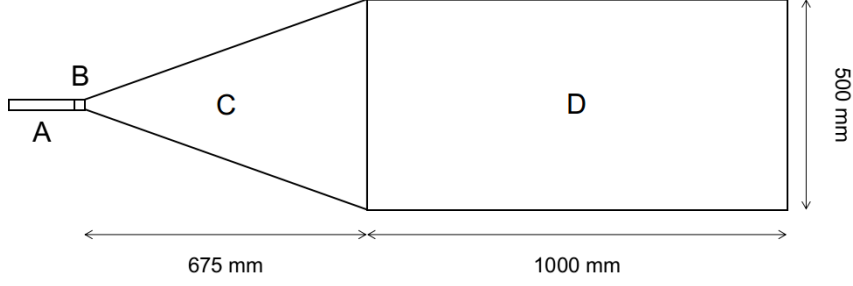


Figure 1.10: Schematic diagram of the HiSPARC scintillation detector. (A): PMT; (B): light-guide adaptor; (C): light-guide; (D): scintillator.

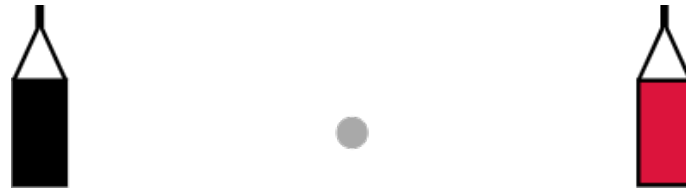
with anthracene as the fluor, and the emission spectrum peaks at a wavelength of 425 nm (Fokkema, 2012; Bartels, 2012). The light-guide is made from Polymethylmethacrylate (PMMA) and has a comparable refractive index to the scintillator (1.58 and 1.49, respectively), reducing refraction effects between the two materials (van Dam et al., 2020).

The PMT used is an ETEnterprises 9125B PMT, with a 25 mm aperture, blue-green sensitive bialkali photocathode, and 11 high-gain dynodes (Bartels, 2012; ETEnterprises, 2020). The quantum efficiency of the PMT used in the HiSPARC detectors peaks at around 375 nm at 28%, and at 425 nm the quantum efficiency is 25% (Fokkema, 2012).

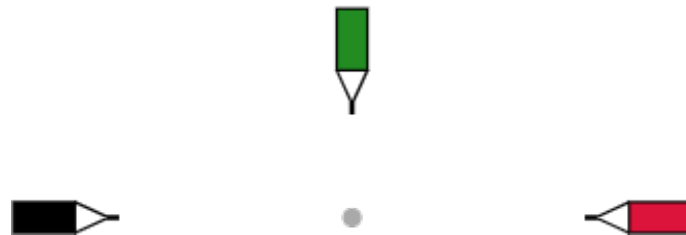
Each detector is wrapped in aluminium foil (thickness 30  $\mu\text{m}$ ) and a black, vinyl material (thickness 0.45 mm), which is usually used as a pond liner, to ensure light-tight detectors and to reduce the noise level from stray photons (van Dam et al., 2020). In addition, each detector is placed inside of its own a plastic roof box to again ensure that it is light-tight, and to also ensure that it is weather-proof, as the detectors are usually located on the roofs of schools, colleges, and universities.

A HiSPARC station combines either 2 or 4 detectors, to observe coincident muons ('events'), and typical configurations of each are shown in Figure 1.11. The separation between detectors varies from station-to-station. In addition some stations have the capability to measure the local atmospheric properties, such as temperature, pressure, relative humidity etc. Moreover, some stations also record the

‘singles’ rates, i.e. the frequency at which an individual detector is triggered, independently of the other detectors in the station. The singles rates are important when investigating non-EAS events.



(a) Two-detector station configuration



(b) Four-detector station configuration (triangle arrangement)



(c) Four-detector station configuration (diamond arrangement)

Figure 1.11: Typical formations of two-detector and four-detector stations. In each, the grey circle denotes a GPS antenna which is located in between the detectors to provide a precise timestamp for each signal.

light pulse which is converted into an electric pulse by the PMT. This pulse is sampled and digitized at 400 MHz

The PMTs of the detector in a station are connected to HiSPARC electronics boxes, which sample and digitise the signal at a rate of 400 MHz, and each PMT is connected to the electronics box using cables of a standard length of 30 m, to minimise any timing offsets between detectors (Fokkema, 2012; van Dam et al., 2020). The electronics boxes are capable of controlling and reading two PMTs, therefore a four-detector station requires two electronics boxes: a master and a slave.

The HiSPARC experiment is set up in such a way as to ensure that each station across the HiSPARC network reads a similar count rate of muons, in order to aid the direct comparison between the different stations in the network. When configuring the station, a trigger threshold must be applied for the PMT signals. This is standardised across the HiSPARC network and can be seen in relation to a detector trigger pulse in Figure 1.12a. There are two thresholds, low: 30 mV, which represents 0.2 of a MIP; high: 70 mV, which represents 0.5 of a MIP (Fokkema, 2012; van Dam et al., 2020). The thresholds were chosen to increase the sensitivity of the stations for observing gamma rays and low energy electrons, but this has the effect of making it more difficult to determine whether an individual detection is from a muon, or another MIP. This is why the HiSPARC network usually relies on detecting ‘events’, from coincident muons.

Each detector in the network is set up such that the pulseheight spectrum peaks at a Most Probable Value (MPV) of  $\sim 150$  mV (see Figure 1.12), and such that the high threshold allows a mean count rate on the order 100 counts per second and the low threshold allows a mean count rate of the order 400 counts per second; these can be tuned by adjusting the PMT voltage. It could be argued that in setting up the detectors in this way, there is an immediate bias in the data to reject lower energy CRs.



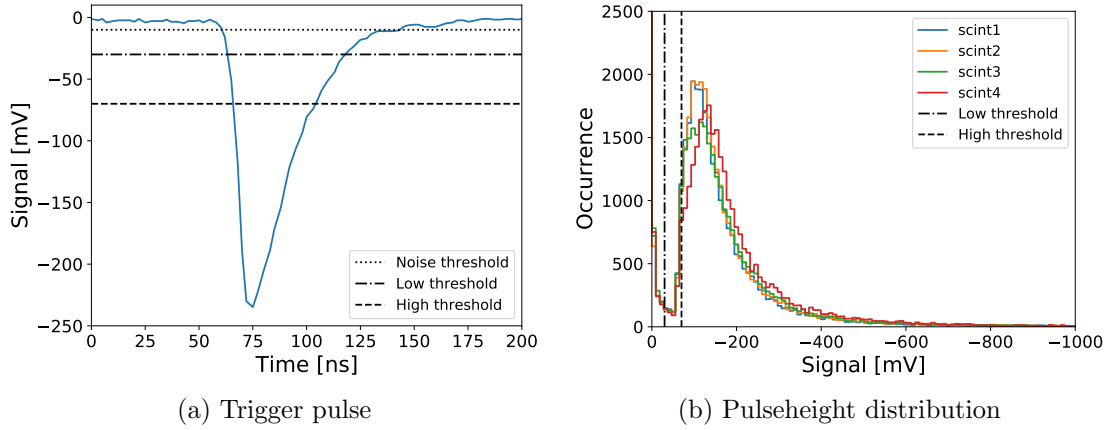


Figure 1.12: (a): An example PMT signal after digital conversion by the HiSPARC electronics box. The horizontal lines denote: the noise cut-off (dotted line), which is used for setting a limit when integrating the pulse height, to give the pulse integral; the low-voltage threshold (dash-dot); the high-voltage threshold (dashed). (b) The pulse height distribution over the course of a single day from HiSPARC station 501. The vertical lines show the low-voltage threshold (dash-dot) and the high-voltage threshold (dashed).

The pulse height spectrum (see Figure 1.12b) is composed of two main regions: the left side which falls off rather steeply and the main, asymmetric part of the spectrum which features a peak and a long tail. The left side of the spectrum is understood to be from high-energy photons (gamma rays) produced in air showers (Fokkema, 2012). These high-energy photons may undergo pair production when interacting with the scintillator which may produce ionising electron and positron pairs. The trigger thresholds are placed to reject these noise signals from the data.

The main, asymmetric distribution which features a peak and a tail is from charged particles (muons and electrons) (van Dam et al., 2020). The mean energy loss of particles in a material is described by the Blethe-Bloch formula; however this does not account for fluctuations in energy loss (Fokkema, 2012). A Landau distribution in fact describes the fluctuations in energy loss of particles. Due to the resolution of the HiSPARC detectors the distribution in Figure 1.12b is best described by the convolution of the Landau distribution with a normal distribution which describes the resolution of the detector (Fokkema, 2012). The peak of the distribution, the most probable values (MPV), is the most likely energy lost by a

particle in the detector, i.e. the 3.51 MeV MIP ([van Dam et al., 2020](#)). It has been shown that the location of the MPV can vary due to the effects of atmospheric temperature ([Bartels, 2012](#); [van Dam et al., 2020](#)).

The default trigger conditions for detecting an air shower event between multiple PMTs within a station differ for a two/four-detector station. In a two-detector station, an event is recorded if the PMT signals from both detectors exceed the low threshold within the coincidence time window ( $1.5\mu\text{s}$ ). In a four-detector station, there are two conditions: (i) at least two detectors exceed the high threshold within the coincidence time window; (ii) at least three detectors exceed the low threshold within the coincidence time window. These are the default conditions, but there are other, user configurable ways of triggering the station.

The scientific goals that can be achieved also vary between the two/four-detector stations. When at least three detectors in a four-detector station observe particles of an EAS, the direction of the EAS (and thus the direction of the PCR) can be acquired using triangulation calculations. When only two detectors in a station observe particles of an EAS, i.e. the limit for a two-detector station, it is only possible to reconstruct the arrival direction along the axis that connects the centres of those two detectors (thus it is not possible to reconstruct the direction of the PCR).

....

## 1.4 The Solar Magnetic Field/Activity/Features...

### 1.4.1 ...

...

comment less here on the smmf but introduce features on the disk...

Solar activity cycle ... ([Hathaway, 2015](#))...

## 1.5 Thesis Structure

In this thesis a number of projects are presented which explore the themes of understanding the solar interior-atmosphere linkage and space weather applications. This is broken down into three major projects: a feasibility study on CR space weather applications, a study into the effects of solar activity on CR observations, and a study of the mean magnetic field of the Sun.

To clarify the structure of this thesis, the contents of each chapter and the main themes within are given in outline, before I present the work in each.

In Chapter ?? ...

Chapter ?? ...

Chapter ?? we studied long-term variations of GCR intensity in relation to the Sun Spot Number (SSN) during the most recent solar cycles ([Ross & Chaplin, 2019](#)). This study analysed the time lag between the GCR intensity and the SSN, and the hysteresis effect of the GCR count rate against SSN for Solar Cycles 20–24.

Chapter ?? deviates away from CR data and instead a frequency-domain analysis of over 20 years of high-cadence Birmingham Solar Oscillations Network (BiSON) observations of the Solar Mean Magnetic Field (SMMF) is presented. We modelled the power spectrum of the BiSON SMMF data to draw conclusions about the morphology of the SMMF, particularly focusing on the source of the rotationally modulated component in the signal.

In Chapter ?? we further investigated the BiSON SMMF data. Here we examined the residual spectrum, after removing our best-fitting model, to search for evidence of a magnetic signature of global Rossby modes ( $r$  modes).

Finally the thesis is concluded in Chapter ...

# Bibliography

- Aab A., et al., 2017, *Science*, 357, 1266
- Andriopoulou M., Mavromichalaki H., Plainaki C., Belov A., Eroshenko E., 2011, *Sol Phys*, 269, 155
- Arunbabu K. P., et al., 2015, *Astronomy and Astrophysics*, 580, A41
- BIS 2015, Space weather preparedness strategy - GOV.UK. Vol. 2.1, <https://www.gov.uk/government/publications/space-weather-preparedness-strategy>
- Bartels R. T., 2012, Technical report, The HiSPARC Experiment: An Analysis of the MPV and the Number of Events per Unit Time. University College Utrecht
- Beggan C., Wild J., Gibbs M., 2018, *A&G*, 59, 4.36
- Belov A. V., 2008, *Proceedings of the International Astronomical Union*, 4, 439
- Belov A. V., Eroshenko E. A., Oleneva V. A., Struminsky A. B., Yanke V. G., 2001, *Advances in Space Research*, 27, 625
- Belov A. V., Eroshenko E. A., Kryakunova O. N., Kurt V. G., Yanke V. G., 2010, *Geomagn. Aeron.*, 50, 21
- Belov A., et al., 2014, *Solar Physics*, 289, 3949
- Bruno A., et al., 2018, *The Astrophysical Journal*, 862, 97
- Cabinet Office 2017, National Risk Register of Civil Emergencies - GOV.UK, 2017 edn. <https://www.gov.uk/government/publications/national-risk-register-of-civil-emergencies-2017-edition>
- Cane H. V., 2000, *Space Science Reviews*, 93, 55
- Cannon P., Royal Academy of Engineering (Great Britain) 2013, Extreme space weather: impacts on engineered systems and infrastructure : summary report
- Chilingarian A., 2003. CERN, Tsakhkadzor, Armenia, pp 63–79, <https://cds.cern.ch/record/604025/files/CERN-2005-007.pdf?page=73>
- Clem J. M., Dorman L. I., 2000, *Space Science Reviews*, 93, 335
- Cramp J. L., 1996, PhD Thesis, University of Tasmania, Hobart, <https://core.ac.uk/download/pdf/33327719.pdf>

- Cramp, J. L. Duldig, M. L. Flckiger, E. O. Humble, J. E. Shea, M. A. Smart, D. F. 1997, *Journal of Geophysical Research: Space Physics*, 102, 24237
- Dorman L. I., 2004a, in *Astrophysics and Space Science Library*, Cosmic Rays in the Earths Atmosphere and Underground. Springer, Dordrecht, pp 289–330, doi:10.1007/978-1-4020-2113-8\_5, [https://link.springer.com/chapter/10.1007/978-1-4020-2113-8\\_5](https://link.springer.com/chapter/10.1007/978-1-4020-2113-8_5)
- Dorman L. I., 2004b, in *Astrophysics and Space Science Library*, Cosmic Rays in the Earths Atmosphere and Underground. Springer, Dordrecht, pp 375–386, doi:10.1007/978-1-4020-2113-8\_7, [https://link.springer.com/chapter/10.1007/978-1-4020-2113-8\\_7](https://link.springer.com/chapter/10.1007/978-1-4020-2113-8_7)
- Duldig M. L., et al., 1993, *Proceedings of the Astronomical Society of Australia*, 10, 211
- Dumbović M., Vršnak B., Čalogović J., Župan R., 2012, *Astronomy & Astrophysics*, 538, A28
- Dumbović M., Vršnak B., Čalogović J., 2016, *Sol Phys*, 291, 285
- Dunai T. J., 2010, in , *Cosmogenic Nuclides: Principles, Concepts and Applications in the Earth Surface Sciences*. Cambridge University Press, Cambridge, pp 1–24, doi:10.1017/CBO9780511804519.003
- ETEnterprises 2020, Technical Report 9125B, Data Sheet: 9125B Series, <http://et-enterprises.com/products/photomultipliers/product/p9125b-series>. ET Enterprises
- Fokkema D. B. R. A., 2012, PhD thesis, University of Twente
- Forbush S. E., 1937, *Physical Review*, 51, 1108
- Gaisser T. K., Engel R., Resconi E., 2016, *Cosmic Rays and Particle Physics*, 2nd edn. Cambridge University Press, doi:10.1017/CBO9781139192194
- Giacalone J., 2010, in Schrijver C. J., Siscoe G. L., eds , *Heliophysics: Space Storms and Radiation: Causes and Effects*. Cambridge University Press, Cambridge, pp 233–262, doi:10.1017/CBO9781139194532.010
- Gloeckler G., 2010, in Schrijver C. J., Siscoe G. L., eds , *Heliophysics: Space Storms and Radiation: Causes and Effects*. Cambridge University Press, Cambridge, pp 233–262, doi:10.1017/CBO9781139194532.004
- Government H., 2020, Risk Register, National Risk Register: 2020 edition, [https://assets.publishing.service.gov.uk/government/uploads/system/uploads/attachment\\_data/file/952959/6.6920\\_CO\\_CCS\\_s\\_National\\_Risk\\_Register\\_2020\\_11-1-21-FINAL.pdf](https://assets.publishing.service.gov.uk/government/uploads/system/uploads/attachment_data/file/952959/6.6920_CO_CCS_s_National_Risk_Register_2020_11-1-21-FINAL.pdf). HM Government
- Gruppen C., 2005, *Astroparticle Physics*. Springer-Verlag, Berlin Heidelberg, doi:10.1007/3-540-27670-X, <https://www.springer.com/gp/book/9783540253129>
- Hathaway D. H., 2015, *Living Rev. Sol. Phys.*, 12, 4

- Homeier N., Wei L., 2013, Technical report, Solar Storm Risk to the North American Electric Grid, <https://www.lloyds.com/news-and-risk-insight/risk-reports/library/natural-environment/solar-storm>. Lloyd's
- Kang J., Jang D. Y., Kim Y., Kang B. H., Kim Y.-K., Kim J., Park H., Yi Y., 2012, *Journal of the Korean Physical Society*, 61, 720
- Knipp D. J., et al., 2016, *Space Weather*, 14, 2016SW001423
- Kuwabara T., et al., 2006a, *Space Weather*, 4, S08001
- Kuwabara T., Bieber J. W., Clem J., Evenson P., Pyle R., 2006b, *Space Weather*, 4, S10001
- Lingri D., Mavromichalaki H., Belov A., Eroshenko E., Yanke V., Abunin A., Abunina M., 2016, arXiv:1612.08900 [astro-ph]
- Lockwood J. A., 1971, *Space Science Reviews*, 12, 658
- McCracken K. G., Moraal H., Shea M. A., 2012, *ApJ*, 761, 101
- MetOffice 2013, Technical Report 13/0402, Space Weather, [https://www.metoffice.gov.uk/binaries/content/assets/mohippo/pdf/public-sector/emergencies/space-weather/space\\_weather\\_datasheet\\_final.pdf](https://www.metoffice.gov.uk/binaries/content/assets/mohippo/pdf/public-sector/emergencies/space-weather/space_weather_datasheet_final.pdf)
- Mishev A. L., Usoskin I. G., Raukunen O., Paassilta M., Valtonen E., Kocharov L. G., Vainio R., 2018, *Solar Physics*, 293
- NOAA 2018, NOAA Space Weather Predictions Center, <https://www.swpc.noaa.gov/>
- Nature 1871, Observations Upon Magnetic Storms in Higher Latitudes, doi:10.1038/004441a0, <https://www.nature.com/articles/004441a0>
- Owens M. J., Forsyth R. J., 2013, *Living Rev. Sol. Phys.*, 10, 5
- Poluianov S., Usoskin I. G., 2017, in Proceedings of Science. Bexco, Busan, Korea, <https://pos.sissa.it/301/#session-3145>
- Poluianov S. V., Usoskin I. G., Mishev A. L., Shea M. A., Smart D. F., 2017, *Sol Phys*, 292, 176
- Poluianov S., Usoskin I., Shea M. A., Smart D. F., 2018, EGU General Assembly Conference Abstracts, 20, 5879
- Riley P., 2012, *Space Weather*, 10
- Rockenbach M., et al., 2014, *Space Sci Rev*, 182, 1
- Ross E., Chaplin W. J., 2019, *Sol Phys*, 294, 8
- Schrijver C. J., Siscoe G. L., eds, 2010, Heliophysics: Space Storms and Radiation: Causes and Effects. Cambridge University Press, Cambridge, doi:10.1017/CBO9781139194532, <https://www.cambridge.org/core/books/heliophysics-space-storms-and-radiation-causes-and-effects/608857F4EEE1C0BF61F26ACD19BA59DE>

- Shea M. A., Smart D. F., 1982, [Space Science Reviews](#), 32, 251
- Simpson J. A., 1948, [Phys. Rev.](#), 73, 1389
- Simpson J. A., Fonger W., Treiman S. B., 1953, [Phys. Rev.](#), 90, 934
- Stoker P. H., Dorman L. I., Clem J. M., 2000, [Space Science Reviews](#), 93, 361
- Strauss R. D., Ogunjobi O., Moraal H., McCracken K. G., Caballero-Lopez R. A., 2017, [Solar Physics](#), 292, 51
- Usoskin I. G., Braun I., Gladysheva O. G., Hörandel J. R., Jmsn T., Kovaltsov G. A., Starodubtsev S. A., 2008, [J. Geophys. Res.](#), 113, A07102
- Usoskin I., Ibragimov A., Shea M. A., Smart D., 2016, in Proceedings of The 34th International Cosmic Ray Conference PoS(ICRC2015). Sissa Medialab, The Hague, The Netherlands, p. 054, [doi:10.22323/1.236.0054](#), <https://pos.sissa.it/236/054>
- Viljanen A., 2011, [Space Weather](#), 9, 07007
- Wawrzynczak A., Alania M. V., 2010, [Advances in Space Research](#), 45, 622
- Zyla, P. A. (Particle Data Group) et al., 2020, [Progress of Theoretical and Experimental Physics](#), 2020
- van Dam K., van Eijk B., Fokkema D. B. R. A., van Holten J. W., de Laat A. P. L. S., Schultheiss N. G., Steijger J. J. M., Verkooijen J. C., 2020, [Nuclear Instruments and Methods in Physics Research Section A: Accelerators, Spectrometers, Detectors and Associated Equipment](#), 959, 163577